


Article

Microstructural Characterization and Mechanical Property of Al-Li Plate Produced by Centrifugal Casting Method

Qingle Tian¹, Kai Deng¹, Zhishuai Xu¹, Ke Han² and Hongxing Zheng^{1,*} 

¹ School of Materials Science and Engineering, Shanghai University, Shanghai 200444, China; qingletian@shu.edu.cn (Q.T.); dengkai@shu.edu.cn (K.D.); xzssh@shu.edu.cn (Z.X.)

² National High Magnetic Field Laboratory, Florida State University, Tallahassee, FL 32310, USA; han@magnet.fsu.edu

* Correspondence: hxzheng@shu.edu.cn; Tel.: +86-21-66136581

Abstract: Using a centrifugal casting method, along with deformation and aging, we produced a high-strength, low-anisotropy Al-Li plate. The electron probe microanalysis, transmission electron microscope, differential scanning calorimetry, and X-ray diffraction were used to clarify the evolution of strengthening phases. Experimental results showed that centrifugal-cast Al-Li plate consisted of intragrain δ' —(Al,Cu)₃Li precipitate and interdendritic θ' —Al₂Cu particles. After cold-rolling to a reduction ratio of 60% and annealing at 800 K for 90 min, both primary θ' and δ' were dissolved in solid solution. Aging at 438 K for 60 h led to the formation of two kinds of precipitates (needle-like T₁—Al₂CuLi and spherical δ' in two sizes), which acted as the main strengthening phases. The average values of ultimate tensile strength and yield strength for the anneal-aged plate reached 496 MPa and 408 MPa, with a total elongation of 3.9%. The anneal-aged plate showed mechanical anisotropy of less than 5%. The tensile fracture morphology indicated a typical intergranular fracture mode.



Citation: Tian, Q.; Deng, K.; Xu, Z.; Han, K.; Zheng, H. Microstructural Characterization and Mechanical Property of Al-Li Plate Produced by Centrifugal Casting Method. *Metals* **2021**, *11*, 966. <https://doi.org/10.3390/met11060966>

Academic Editor: Paolo Ferro

Received: 19 May 2021
Accepted: 14 June 2021
Published: 16 June 2021

Publisher's Note: MDPI stays neutral with regard to jurisdictional claims in published maps and institutional affiliations.



Copyright: © 2021 by the authors. Licensee MDPI, Basel, Switzerland. This article is an open access article distributed under the terms and conditions of the Creative Commons Attribution (CC BY) license (<https://creativecommons.org/licenses/by/4.0/>).

Keywords: Al-Li alloy; centrifugal casting; microstructure; mechanical property

1. Introduction

Al-Li alloys are attractive for military and aerospace applications because of their higher ratio of strength to density than other Al alloys [1–5]. This superior property is principally attributed to Li element added to α —Al matrix, where 1 wt.% addition of Li would reduce the density by approximately 3% and increase the elastic modulus by 6% [6]. The development of Al-Li alloys can be roughly divided into three stages [7,8]. The first stage spanned from the 1950s to the early 1960s, and the representative 2020 alloy was produced by Alcoa of the United States. The alloy was used as both wing skin and tail horizontal stabilizer of the military warning aircraft, achieving a weight reduction of 6% [4]. In the mid-1960s, the second-generation Al-Li alloys, including 1420 alloy developed by the former Soviet Union [9], 2090 alloy by Alcoa of the United States [10], 8090 and 8091 alloys by Alcan of the United Kingdom [11], successfully replaced most of 2xxx Al parts owing to their low density and high elastic modulus. However, severe anisotropy and bad weldability hinder their competitiveness with 7xxx Al alloys [12]. In the late 1980s, the third-generation Al-Li alloys, represented by the American Weldalite049 series alloys, were developed [13,14]. These alloys had improved weldability.

Vacuum liquid metallurgy method has been widely used for the syntheses of Al-Li ingot. The first key issue is the composition inhomogeneity resulting from the extremely high chemical activity of Li element [15–19]. Researchers used powder metallurgy to improve the homogeneity [20]. The powder metallurgy, however, had limited application because of the high costs involved. Another pivotal issue lies in the mechanical anisotropy caused by severe plastic deformation, which is necessary for the enhancement of strength and ductility. Presently it has been well accepted that the mechanical anisotropy is mainly linked to the deformation-induced crystallographic texture and the texture or anisotropy

due to precipitate dislocation interactions [21]. In the present work, a sub-rapidly solidified Al-Li plate was prepared at a high cooling rate up to 1000 K/s by using the centrifugal casting method. Under a high cooling rate, it was generally expected to expand the solid solubility limit and to refine the microstructure for the sub-rapidly solidified plate [22]. The evolution of strengthening phases was investigated and the main objective is to explore a new approach to produce high-strength Al-Li plates.

2. Materials and Methods

A commercial hot-rolled Al-Li 2A97 sheet in the form of 50 mm-thick supplied by Aluminum Corporation of China was used in the present study. The chemical composition of commercial hot-rolled Al-Li sheet is listed in Table 1. The alloy of 65 g was rapidly remelted within a top-open quartz tube by induction. After the bottom BN baffle was removed, the levitating melt was dropped into a high-speed rotary centrifugal copper mold ($w = 600$ rpm) through a graphitic funnel (Figure 1). A centrifugal-cast Al-Li plate with a dimension of 60 mm (length) \times 40 mm (width) \times 2.5 mm (thickness) was obtained. The cooling rate was estimated up to 1000 K/s. The details of the experimental procedure have been reported by Xu et al. [23]. The centrifugal-cast plate was further cold-rolled to 1.0 mm-thick with single pass reduction of about 0.15 mm. The cold-rolled plate was then sealed in a quartz tube and annealed at 800 K for 90 min, followed by aging at 438 K for 60 h. Hereinafter, we referred to it as “anneal-aged plate” for the annealed and aged plate.

Table 1. Chemical composition of investigated Al-Li sheet (wt.%).

Cu	Li	Mg	Zn	Mn	Zr	Al
3.85	1.50	0.45	0.46	0.30	0.13	balance

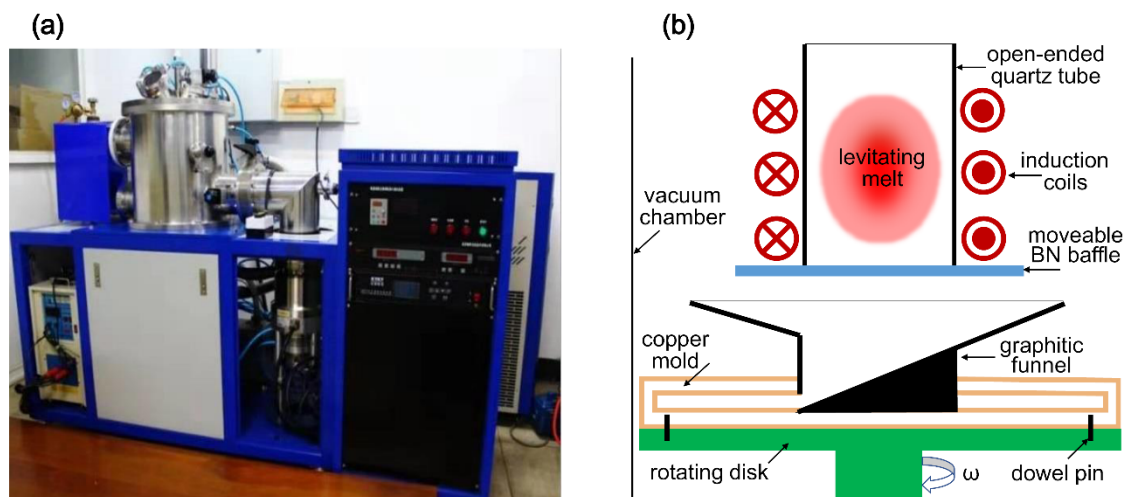


Figure 1. Self-designed centrifugal casting setup (a) and the schematic diagram (b).

Microstructure was observed using electron probe microanalysis (EPMA-8050G, Shimadzu, Tokyo, Japan) with a wave dispersive spectrometer (WDS, Bruker Corporation, Harvard, MA, USA). Conventional transmission electron microscopic (TEM, JEOL Ltd., Tokyo, Japan) observations were conducted on a JEM-2100F with an energy dispersive spectrometer (EDS, Bruker Corporation, Harvard, MA, USA). HAADF-STEM was performed on a FEI Tecnai G2 F20 instrument (Thermo Fisher Scientific Inc., Hillsboro, OR, USA) operating at a voltage of 200 kV. Thin foils were prepared by twin-jet electropolishing in a Tenupol-3 instrument (Struers Inc., Cleveland, OH, USA) at 20 V, and a solution of 30 vol.% nitric acid and 70 vol.% methanol (cooled to -30 °C) was used. X-ray diffraction (XRD, DImax-2500, Rigaku, Osaka, Japan) with Cu $K\alpha$ radiation was employed to detect the phase structure.

Differential scanning calorimetric measurement (DSC, Netzsch 404 F3, NETZSCH-Gerätebau GmbH, Selb, Germany) was carried out at a heating rate of 20 K/min.

Three tensile specimens with a dimension of 30 mm (length) \times 5 mm (width) \times 1 mm (thickness) were taken from the anneal-aged plate by wire electro-discharge machining method along rolling direction (RD) and transverse direction (TD), respectively. All surfaces were mechanically ground with a 2000-grit SiC abrasive paper prior to the tensile testing. A mini-extensometer (Epsilon 3442, Epsilon Technology Corp., Jackson, WY, USA) with a gauge length of 6 mm was employed. Mechanical properties were evaluated using a tensile testing machine (MTS C44, MTS System, Eden Prairie, MN, USA) at a strain rate of 10^{-3} /s.

3. Results and Discussion

Back scattered electron (BSE) imaging of a centrifugal-cast sample showed refined dendritic α -Al with a grain size of $14.5 \pm 0.2 \mu\text{m}$ (Figure 2a), which was different from the coarse dendrite structure with severe dendritic segregation in the vacuum induction melted Al-Li alloy [24,25]. The enlarged BSE image showed sub-microscale white interdendritic particles concentrated along grain boundaries with many greyish nanoscale particles inhomogeneously distributed within the grains (Figure 2b). EPMA results showed that the white particles along grain boundaries contained more Cu than α -Al matrix (Figure 2c,d).

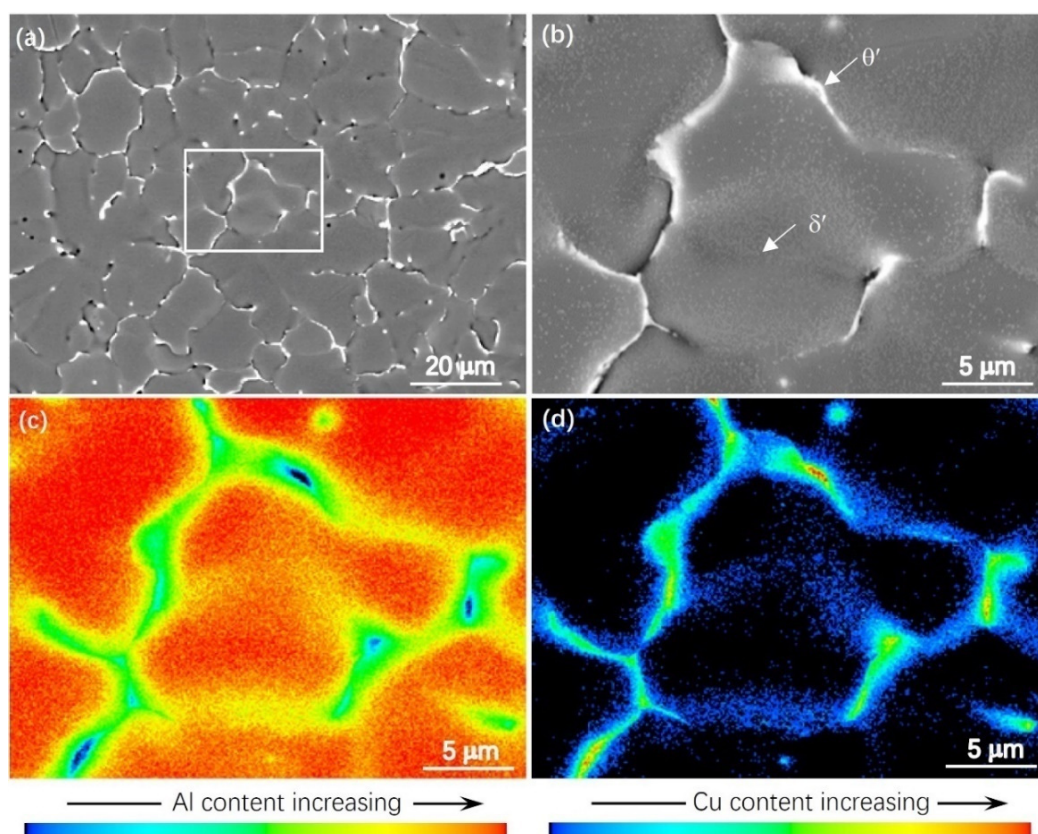


Figure 2. BSE images (a,b) of produced centrifugal-cast sample, (c,d) are WDS elemental maps of Al and Cu corresponding to (b), respectively.

HADDF-STEM images and EDS elemental analysis showed intragrain Cu-containing nanoparticles in clusters averaging 30 nm in size (Figure 3). Selected area diffraction patterns (SADPs) from the regions highlighted by red circles revealed the presence of θ' - Al_2Cu for the interdendritic particles and δ' - $(\text{Al,Cu})_3\text{Li}$ for the intragrain nanoparticles [26]. Given that we used cooling rates up to 1000 K/s for the centrifugal-cast sample, we assumed that the θ' particles formed from the residual liquid during the final solidification stage and that the δ' particles precipitated from supersaturated α -Al matrix.

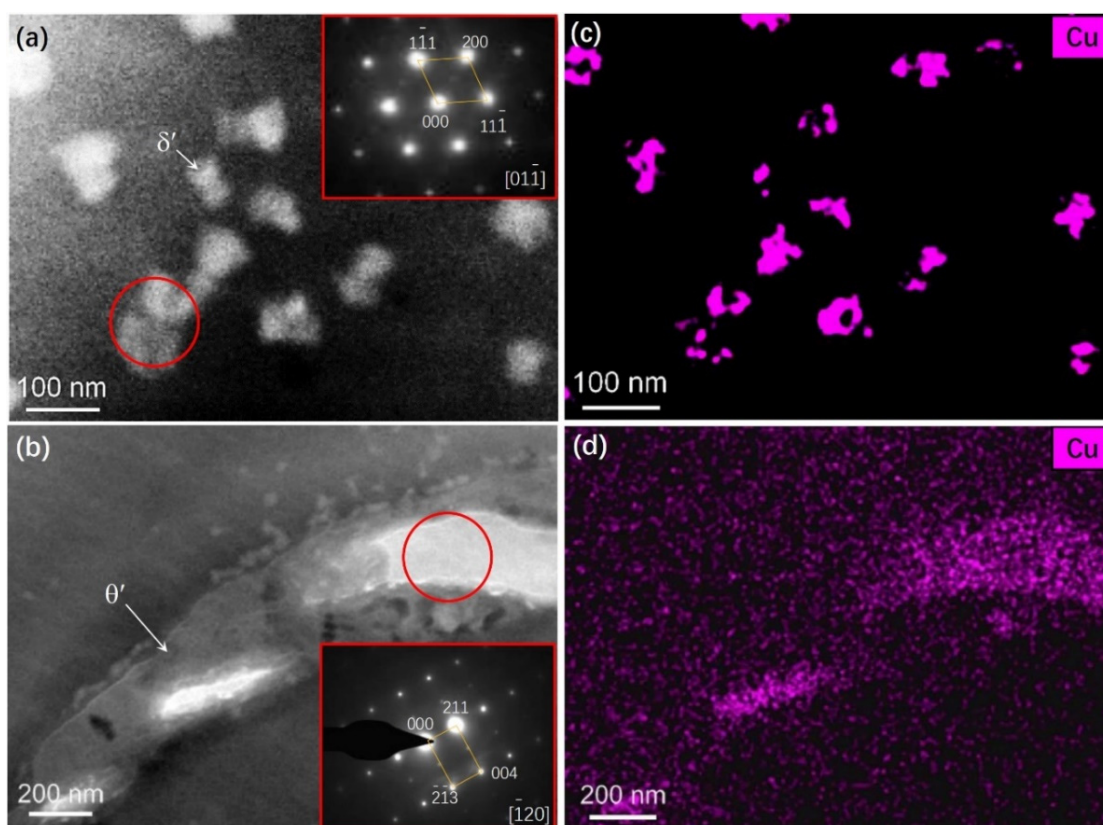


Figure 3. HADDF-STEM images taken from intragrain (a) and from grain boundary (b) of centrifugal-cast sample. Inserted SADPs from regions highlighted by red circles, indicating presence of δ' — $(\text{Al,Cu})_3\text{Li}$ and θ' — Al_2Cu , respectively. (c,d) showing corresponding EDS elemental maps of Cu.

After cold rolling the centrifugal-cast sample to a thickness of 1 mm, the dendritic α -Al grains stretched out into elongated oval shapes (Figure 4a). Many of the brittle θ' particles along grain boundaries were broken into smaller particles or discontinuous strips. Because of the brittleness of the θ' particles and the weak bonding between θ' and α -Al matrix, micro-voids formed close to the θ' particles (Figure 4b). The primary δ' particles almost disappeared.

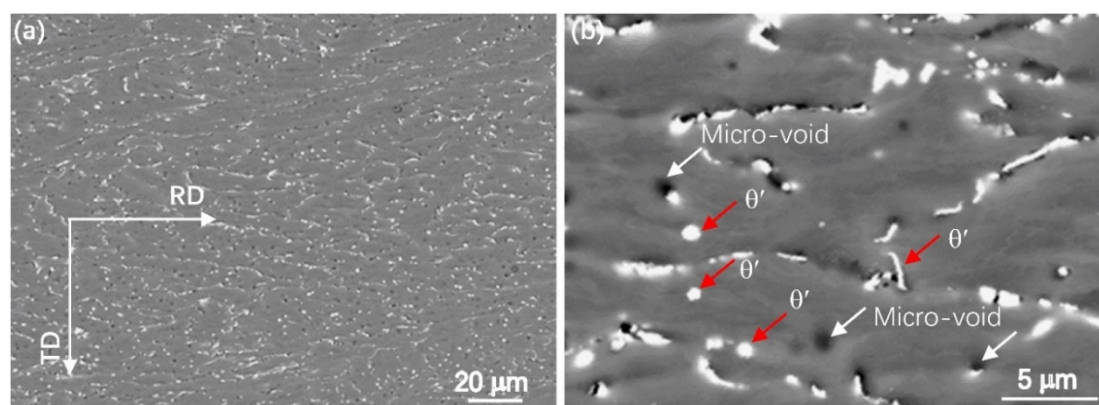


Figure 4. BSE image of the cold-rolled sample (a) (RD: rolling direction, TD: transverse direction), enlarged image (b) showing broken θ' — Al_2Cu marked by red arrows and micro-voids marked by white arrows.

After the cold-rolled sample was further annealed at 800 K for 90 min, the TEM bright-field image (Figure 5a) showed the appearance of one type of precipitates, and the SADP

taken from the area highlighted by a red circle confirmed that the particles were δ' phase (Figure 5b).

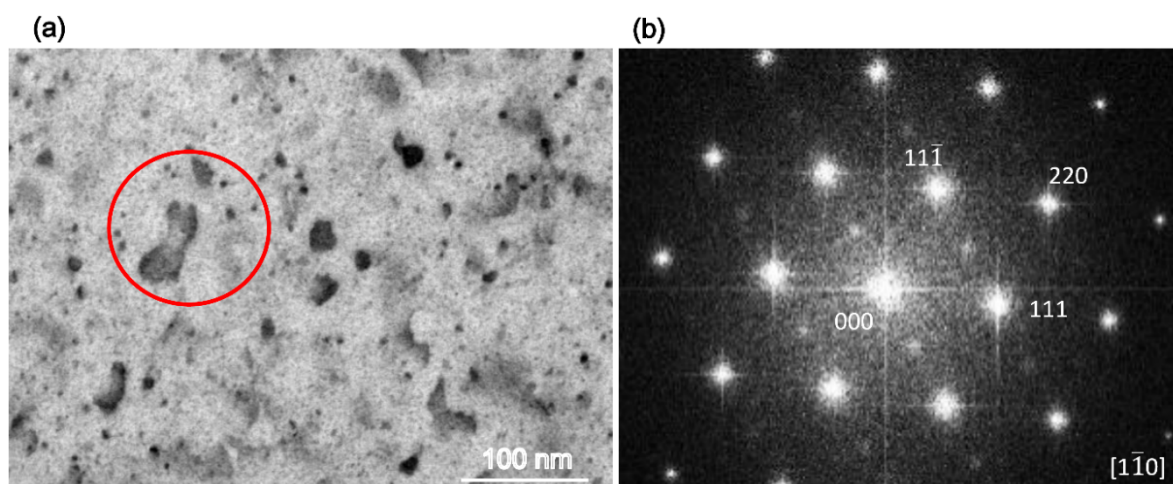


Figure 5. TEM bright-field image of annealed sample (a) and the SADP taken from the highlighted area by red circle (b).

After the cold-rolled sample was annealed at 800 K for 90 min and aged at 438 K for 60 h, BSE images revealed that the elongated α -Al grains recrystallized into equiaxed matrix grains with an average size of 40 μm , with white particles distributed homogeneously in the matrix. BSE image also indicated that almost all the primary θ' phase dissolved (Figure 6a,b). TEM image (Figure 6c) showed three types of precipitates: (1) larger round particles with an average diameter of 42 nm; (2) smaller round particles, about 10–15 nm; (3) thin needle-like precipitates. SADP from the area highlighted by the red circle confirmed that these round particles were all δ' phase (Figure 6d) [27]. EDS elemental analysis indicated that these particles were all rich in Cu (Figure 6e). δ' phase appeared in both centrifugal-cast and anneal-aged samples. However, while they appeared in clusters after centrifugal-casting, separate particles were observed after annealing and aging. The needle-like precipitates were T_1 -Al₂CuLi [28] according to the morphology and EDS analysis as well (Figure 6f). The nucleation and growth of T_1 were brought about by deformation-induced dislocations in the α -Al matrix that occurred during cooling after annealing [29], which was in agreement with the result shown in Figure 5.

XRD patterns for a centrifugal-cast sample and an anneal-aged sample revealed the phase transformations associated with these two fabrication stages (Figure 7a). Diffraction peaks closely corresponded to the standards for α -Al, θ' , δ' , and T_1 [27]. The diffraction peak of θ' at $2\theta = 43.87^\circ$ appeared in the centrifugal-cast sample but disappeared in the anneal-aged sample. Meanwhile, the diffraction peak from T_1 phase at $2\theta = 39.77^\circ$ was absent from the centrifugal-cast sample but appeared in the anneal-aged sample. In the centrifugal-cast sample, peaks of δ' at $2\theta = 65.32, 78.53,$ and 82.73° were separated from peaks of the α -Al matrix at similar angles, indicating slight misfit between precipitates and matrix. Using the least-squares method, the lattice parameters of α -Al and δ' in the centrifugal-cast sample were calculated to be 0.4057 and 0.4029 nm, respectively. This 0.7% misfit can be attributed to a lower energy barrier for the formation of δ' from α -Al supersaturated solid solution during rapid solidification [30]. In the anneal-aged sample, however, peaks of θ' at $2\theta = 65.00, 78.19,$ and 82.34° were overlapped with peaks from the α -Al matrix at similar angles, indicating that coherent precipitates were forming at an early stage of aging. In the anneal-aged sample, a shift of the peaks toward lower angles in the α -Al phase indicated that dissolving more alloying elements into matrix expanded the volume of each α -Al unit-cell ($a = 0.4068$ nm) [31]. Those extra dissolved alloying elements came mainly from the dissolution of primary θ' during annealing at 800 K, a temperature that corresponds to the endothermic peak, in the vicinity of 792 K [32], measured during heating in our DSC experiment (Figure 7b). In the anneal-aged sample, the endothermic peak vanished. We propose that the

two kinds of δ' particles are formed at different temperatures. The larger ones either formed during cooling after annealing or resulted from partially dissolved primary δ' particles, while the smaller ones nucleated during aging at 438 K. In both cases, the endothermic peak of δ' is not visible due to small volume.

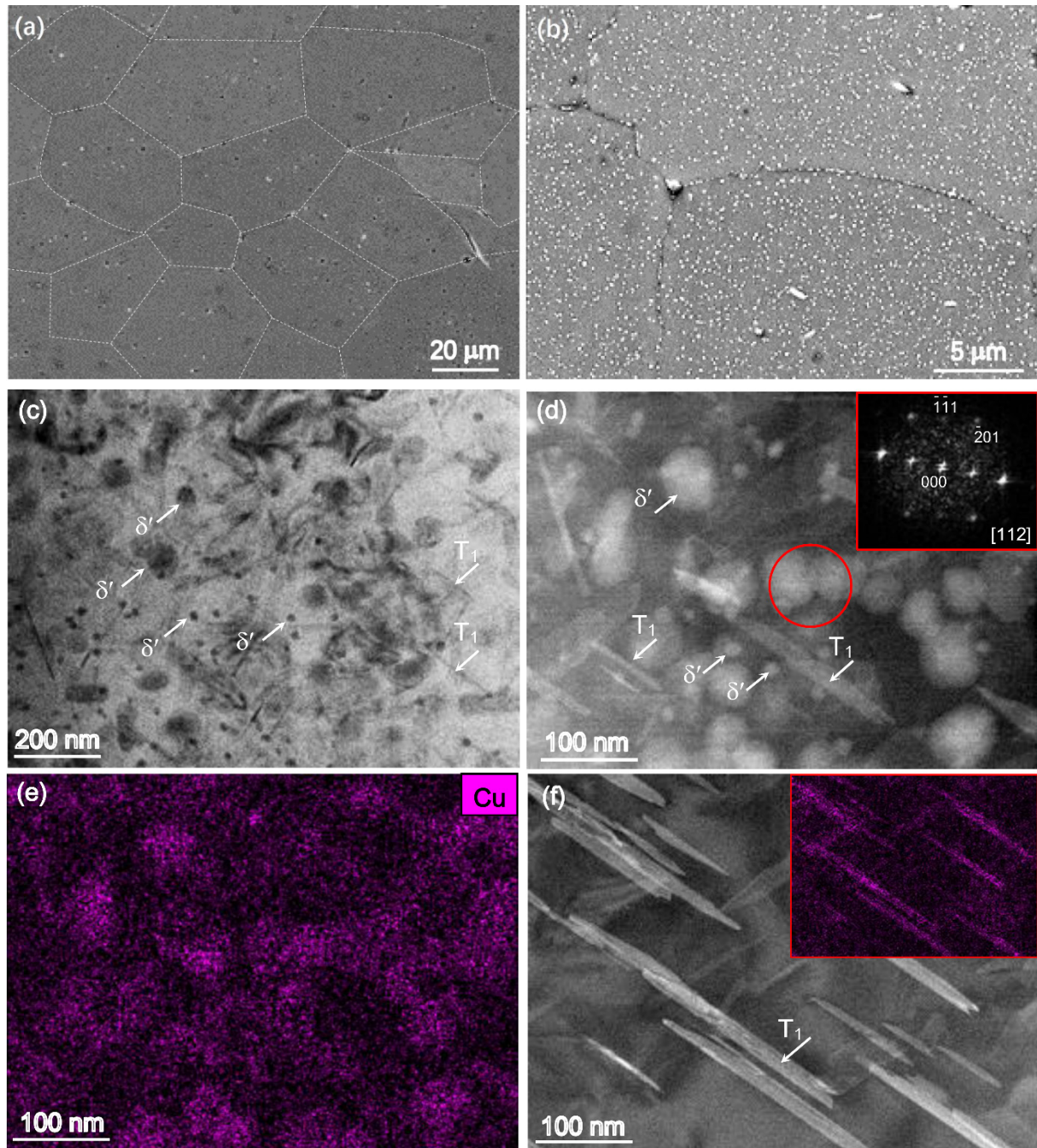


Figure 6. BSE images (a,b) and TEM bright-field image (c), STEM dark-field image and SADP (area highlighted by red circle) (d), and the corresponding EDS elemental map of Cu (e), STEM dark-field image and inserted EDS elemental map of Cu (f) of anneal-aged sample. Round δ' particles and needle-like T_1 precipitates are pointed by white arrows in (c,d,f). Dashed line was drawn along grain boundaries in (a) for clarity.

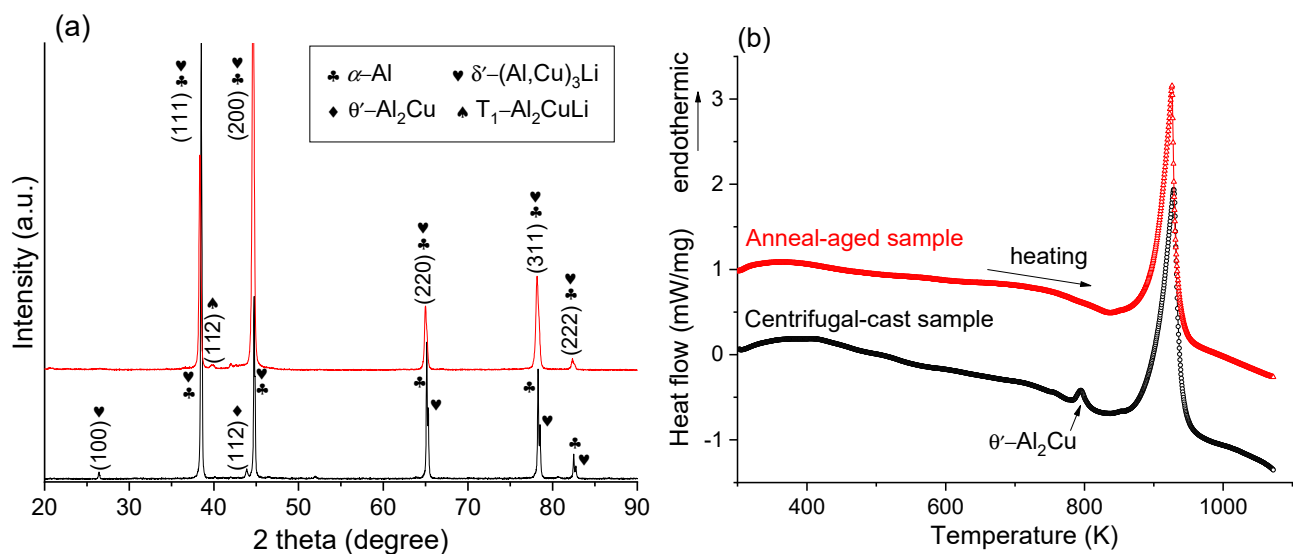


Figure 7. XRD patterns (a) and DSC charts (b) of centrifugal-cast sample (lower) and anneal-aged sample (upper).

Data from tensile tests along RD and TD of samples taken from the anneal-aged plate showed that the average values of ultimate tensile strength (UTS) and yield strength (YS) reached up to 496 and 408 MPa, respectively (Table 2). These values were higher than those of cold-rolled commercial 2A97 alloys (RD: UTS = 448 MPa, YS = 411 MPa; TD: UTS = 443 MPa, YS = 389 MPa) reported by Yu et al. [33]. The average value of total elongation (TEL) of samples was 3.9% (RD: TEL = 3.8%; TD: TEL = 4.0%), lower than the average value (14.7%) (RD: TEL = 17.6%; TD: TEL = 11.8%) [33]. It is assumed that the presence of high density δ' and T_1 precipitates led to an 11% increase in UTS. It is speculated that the coarsening of both these precipitates and the α -Al grains in the samples may cause the observed 70% decrease in TEL, even though both precipitates were homogeneously distributed. With that in mind, we would suggest systematic optimization of rolling and annealing processes in order to improve the properties of finished products.

Table 2. Mechanical properties of tensile specimens taken along different directions.

	UTS (MPa)	YS (MPa)	TEL (%)
RD specimen	506 ± 11	418 ± 10	3.8 ± 0.15
TD specimen	487 ± 8	398 ± 8	4.0 ± 0.20
Average value	496	408	3.9

The anisotropy in the mechanical properties of the anneal-aged sample was below 5%. The RD specimens possessed a slightly higher UTS (3.8% increase) and YS (4.8% increase), and lower TEL (5.0% decrease), compared to the TD specimens. This pattern, with higher strength in RD accompanied by lower anisotropy, differs from alloys in which the relationship is reversed, and could thus be beneficial in certain engineering applications [34–38]. We speculate that the low plastic deformation (i.e., 60% cold-rolling reduction ratio) led to weak mechanical anisotropy. This is different from the conventional liquid metallurgy method used to produce Al-Li sheets, a method involving severe plastic deformation to high strain, including both hot rolling and cold rolling. High strain deformation introduces a texture that is too strong to be fully eliminated by post-annealing, meaning that strong anisotropy occurs [39]. In our samples, partial recovery and recrystallization during annealing produced equiaxed grains that evolved from cold-rolled elongated α -Al grains (Figure 6a,b).

Fracture surface examination indicated that no clear macro-necking occurred during any of the tensile tests, which was in accordance with their low plasticity (Figure 8a). The appearance of dense crack branching and a few equiaxed dimples indicated a quasi-cleavage intergranular fracture, a characteristic typical of Al-Li alloys (Figure 8b) [40,41].

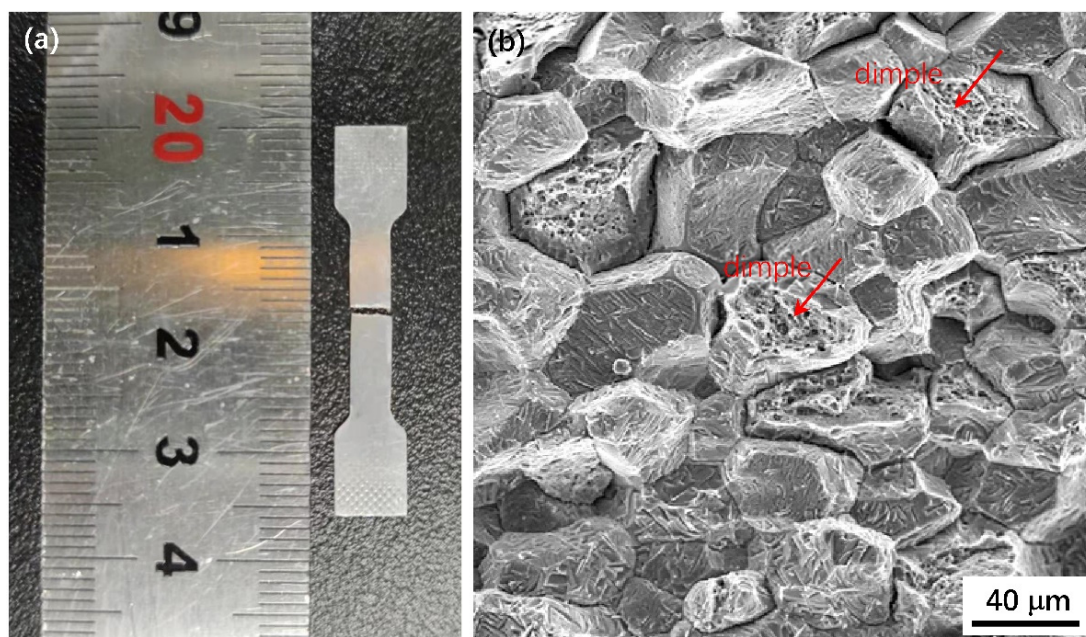


Figure 8. Macro-fracture (a) and surface morphology (b) of anneal-aged tensile specimen.

4. Conclusions

This paper shows how a centrifugal casting method can be used to produce homogeneously high-strength Al-Li plate. After the annealing and aging of cold-rolled centrifugal-cast samples, most of the primary θ' — Al_2Cu and δ' — $(\text{Al,Cu})_3\text{Li}$ precipitates had dissolved in solid solution, leaving two kinds of precipitate, needle-like T_1 — Al_2CuLi and spherical δ' in two sizes, the larger round particles with an average diameter of 42 nm and the smaller round particles, about 10–15 nm. These precipitates acted as the main strengthening phases in the anneal-aged plate. The values of UTS and YS were higher than cold-rolled commercial alloys of similar chemistry, but the elongation was lower. The resulting anneal-aged plate showed uniform mechanical properties with less than 5% difference between rolling direction and transverse direction.

Author Contributions: Conceptualization, Q.T. and H.Z.; methodology, Q.T. and H.Z.; validation, Q.T., K.D. and Z.X.; formal analysis, Q.T., K.D., Z.X. and K.H.; investigation, Q.T., K.D., Z.X. and K.H.; resources, Q.T.; data curation, Q.T., K.D., Z.X. and K.H.; writing—original draft preparation, Q.T. and K.D.; writing—review and editing, K.H. and H.Z.; visualization, Q.T. and H.Z.; supervision, H.Z.; project administration, H.Z.; funding acquisition, H.Z. and K.H. All authors have read and agreed to the published version of the manuscript.

Funding: This research was funded by the National Natural Science Foundation of China (Grants No. 52074180 and 51904182), the Key Program of Science and Technology of Yunnan Province (Grant No. 202002AB080001-2) and the National Science Foundation of USA (Grant No. DMR-1644779).

Acknowledgments: A portion of this work was performed at the National High Magnetic Field Laboratory (NHMFL), USA. The authors are also thankful to Mary Tyler for editing.

Conflicts of Interest: The authors declare no conflict of interest.

References

1. El-Aty, A.A.; Xu, Y.; Zhang, S.H.; Ma, Y.; Chen, D.Y. Experimental investigation of tensile properties and anisotropy of 1420, 8090 and 2060 Al-Li alloys sheet undergoing different strain rates and fiber orientation: A comparative study. *Procedia Eng.* **2017**, *207*, 13–18. [[CrossRef](#)]
2. Betsofen, S.Y.; Antipov, V.V.; Knyazev, M.I. Al-Cu-Li and Al-Mg-Li alloys: Phase composition, texture, and anisotropy of mechanical properties (Review). *Russ. Met. Met.* **2016**, *4*, 326–341. [[CrossRef](#)]

3. El-Aty, A.A.; Xu, Y.; Guo, X.Z.; Zhang, S.H.; Ma, Y.; Chen, D.Y. Strengthening mechanisms, deformation behavior, and anisotropic mechanical properties of Al-Li alloys: A review. *J. Adv. Res.* **2018**, *10*, 49–67. [CrossRef] [PubMed]
4. Rioja, R.J.; Liu, J. The evolution of Al-Li base products for aerospace and space applications. *Met. Mater. Trans. A* **2012**, *43*, 3325–3337. [CrossRef]
5. Yuan, T.; Wu, Y.; Liang, Y.; Jiao, Q.N.; Zhang, Q.C.; Jiang, J.H. Microstructural control and mechanical properties of a high Li-containing Al-Mg-Li alloy. *Mater. Charact.* **2021**, *172*, 110895. [CrossRef]
6. Li, J.F.; Zheng, Z.Q.; Ren, W.D.; Chen, W.J.; Zhao, X.S.; Li, S.C. Simulation on function mechanism of T₁(Al₂CuLi) precipitate in localized corrosion of Al-Cu-Li alloys. *Trans. Nonferr. Met. Soc. China* **2006**, *16*, 1268–1273. [CrossRef]
7. Dursun, T.; Soutis, C. Recent developments in advanced aircraft aluminum alloys. *Mater. Des.* **2014**, *56*, 862–871. [CrossRef]
8. Starke, E.A. Chapter 1-Historical Development and Present Status of Aluminum-Lithium Alloys. In *Aluminum-lithium Alloys, Processing, Properties and Applications*; Prasad, N.E., Gokhale, A.A., Wanhill, R.J.H., Eds.; Butterworth-Heinemann, Elsevier: Amsterdam, The Netherlands, 2014; pp. 3–26.
9. Rioja, R.J. Fabrication methods to manufacture isotropic Al-Li alloys and products for space and aerospace applications. *Mater. Sci. Eng. A* **1998**, *257*, 100–107. [CrossRef]
10. Fridlyander, I.N. Structural aluminum-lithium alloys. *Met. Sci. Heat Treat.* **1990**, *32*, 235–245. [CrossRef]
11. Wanhill, R.J.H.; Bray, G.H. Chapter 2-Aerostructural Design and Its Application to Aluminum-Lithium Alloys. In *Aluminum-lithium Alloys, Processing, Properties and Applications*; Prasad, N.E., Gokhale, A.A., Wanhill, R.J.H., Eds.; Butterworth-Heinemann, Elsevier: Amsterdam, The Netherlands, 2014; pp. 27–58.
12. Sugamata, M.; Blankenship, C.P.; Starke, E.A. Predicting plane strain fracture toughness of Al-Li-Cu-Mg alloys. *Mater. Sci. Eng. A* **1993**, *163*, 1–10. [CrossRef]
13. Pickens, J.R.; Heubaum, F.H.; Kramer, L.S.; Kumar, S.K. Ultra High Strength Weldable Aluminum-Lithium Alloys. U.S. Patent US5032359A, 16 July 1991. Available online: <https://www.freepatentsonline.com/5032359.html> (accessed on 16 June 2021).
14. Muzzolini, R. FEA optimizes airframe panels. *Adv. Mater. Process.* **2005**, *163*, 37–39. Available online: <https://www.asminternational.org/documents/10192/1898536/amp16311p037.pdf/18de88a8-ce72-490c-9340-bd83467a569a> (accessed on 16 June 2021).
15. Sun, Z.Y.; Tian, X.J.; He, B.; Li, Z.; Tang, H.B. Microstructure evolution and microhardness of the novel Al-Cu-Li-xSc alloys fabricated by laser rapid melting. *Vacuum* **2021**, *189*, 110235. [CrossRef]
16. Wu, L.; Li, X.; Wang, H. The effect of major constituents on microstructure and mechanical properties of cast Al-Li-Cu-Zr alloy. *Mater. Charact.* **2021**, *171*, 110800. [CrossRef]
17. Qin, S.; Lee, S.; Tsuchiya, T.; Matsuda, K.; Horita, Z.; Kocisko, R.; Kvackaj, T. Aging behavior of Al-Li-(Cu, Mg) alloys processed by different deformation methods. *Mater. Des.* **2020**, *196*, 109139. [CrossRef]
18. Liu, D.Y.; Ma, Y.L.; Li, J.F.; Zhang, R.F.; Iwaoka, H.; Hirosawa, S. Precipitate microstructures, mechanical properties and corrosion resistance of Al-1.0 wt% Cu-2.5 wt% Li alloys with different micro-alloyed elements addition. *Mater. Charact.* **2020**, *167*, 110528. [CrossRef]
19. Gharbi, O.; Birbilis, N.; Ogle, K. Li reactivity during the surface pretreatment of Al-Li alloy AA2050-T3. *Electrochim. Acta* **2017**, *243*, 207–219. [CrossRef]
20. Kim, S.S.; Shin, K.S. Closure-affected fatigue crack propagation behaviors of powder metallurgy-processed Al-Li alloys in various environments. *Met. Mater. Trans. A* **1999**, *30*, 2097–2102. [CrossRef]
21. Kolobov, Y.P.; Naidenkin, E.V.; Dudarev, E.F.; Bakach, G.P.; Pochivalov, Y.I.; Girsova, N.V.; Ivanov, M.B. The effect of severe plastic deformation on the structure and mechanical properties of Al-Mg-Li alloys. *Russ. Phys. J.* **2002**, *45*, 453–457. [CrossRef]
22. Zhang, J.; Hu, C.; Zhang, Y.; Li, J.; Song, C.; Zhai, Q. Microstructures, mechanical properties and deformation of near-rapidly solidified low-density Fe-20Mn-9Al-1.2C-xCr steels. *Mater. Des.* **2020**, *186*, 108307. [CrossRef]
23. Xu, Z.; Dai, Y.; Fang, Y.; Luo, Z.; Han, K.; Song, C.; Zhai, Q.; Zheng, H. High-temperature phase transition behavior and magnetocaloric effect in a sub-rapidly solidified La-Fe-Si plate produced by centrifugal casting. *J. Mater. Sci. Technol.* **2018**, *34*, 1337–1343. [CrossRef]
24. Yang, S.L.; Shen, J.; Yan, X.D.; Li, X.W.; Zhang, F.; Sun, B. Homogenization treatment parameter optimization and microstructural evolution of Al-Cu-Li alloy. *Rare Metal Mat. Eng.* **2017**, *46*, 28–34. [CrossRef]
25. Nayan, N.; Govind, S.N.K.; Mittal, M.C.; Sudhakaran, K.N. Studies on Al-Cu-Li-Mg-Ag-Zr alloy processed through vacuum induction melting (VIM) technique. *Mater. Sci. Eng. A* **2007**, *454–455*, 500–507. [CrossRef]
26. Wu, L.; Zhou, C.; Li, X.; Ma, N.; Wang, H. Microstructural evolution and mechanical properties of cast high-Li-content TiB₂/Al-Li-Cu composite during heat treatment. *J. Alloys Compd.* **2018**, *739*, 270–279. [CrossRef]
27. Rodak, K.; Urbańczyk-Gucwa, A.; Jabłońska, M.; Pawlicki, J.; Mizera, J. Influence of heat treatment on the formation of ultrafine-grained structure of Al-Li alloys processed by SPD. *Arch. Civ. Mech. Eng.* **2018**, *18*, 331–337. [CrossRef]
28. Cassada, W.A.; Shiflet, G.J.; Starke, E.A. Mechanism of Al₂CuLi (T₁) nucleation and growth. *Met. Mater. Trans. A* **1991**, *22*, 287–297. [CrossRef]
29. Cassada, W.A.; Shiflet, G.J.; Starke, E.A. The effect of plastic deformation on Al₂CuLi (T₁) precipitation. *Met. Mater. Trans. A* **1991**, *22*, 299–306. [CrossRef]
30. Noble, B.; Bray, S.E. On the α(Al)/δ'(Al₃Li) metastable solvus in aluminum-lithium alloys. *Acta Mater.* **1998**, *46*, 6163–6171. [CrossRef]

31. Xi, S.; Zuo, K.; Li, X.; Ran, G.; Zhou, J. Study on the solid solubility extension of Mo in Cu by mechanical alloying Cu with amorphous Cr(Mo). *Acta Mater.* **2008**, *56*, 6050–6060. [[CrossRef](#)]
32. Sidhar, H.; Mishra, R.S. Aging kinetics of friction stir welded Al-Cu-Li-Mg-Ag and Al-Cu-Li-Mg alloys. *Mater. Des.* **2016**, *110*, 60–71. [[CrossRef](#)]
33. Yu, J.; Lu, Z.; Xiong, Y.C.; Li, G.A.; Feng, Z.H. Effect of intermediate thermomechanical treatment on microstructure and mechanical properties of 2A97 Al-Li alloy. *Mater. Sci. Forum* **2019**, *960*, 70–77. [[CrossRef](#)]
34. Ishmaku, A.; Han, K. Characterization of cold-rolled and aged MP35N alloys. *Mater. Charact.* **2001**, *47*, 139–148. [[CrossRef](#)]
35. Ishmaku, A.; Han, K. Deformation induced nanostructure and texture in MP35N alloys. *J. Mater. Sci.* **2004**, *39*, 5417–5420. [[CrossRef](#)]
36. Ishmaku, A.; Han, K.P. Characterization of cold-rolled Cu-Nb composite. *Mater. Sci. Forum* **2004**, *453–454*, 479–484. [[CrossRef](#)]
37. Davy, C.A.; Han, K.; Kalu, P.N.; Bole, S.T. Examinations of Cu-Ag composite conductors in sheet forms. *IEEE Trans. Appl. Supercond.* **2008**, *18*, 560–563. [[CrossRef](#)]
38. Han, K.; Toplosky, V.J.; Goddard, R.; Lu, J.; Niu, R.; Chen, J.P. Impacts of heat treatment on properties and microstructure of Cu16at% Ag conductors. *IEEE Trans. Appl. Supercond.* **2011**, *22*, 6900204. [[CrossRef](#)]
39. Jiang, B.; Cao, F.; Wang, H.; Yi, D.; Jiang, Y.; Shen, F.; Wang, B.; Liu, H. Effect of aging time on the microstructure evolution and mechanical property in an Al-Cu-Li alloy sheet. *Mater. Sci. Eng. A* **2019**, *740–741*, 157–164. [[CrossRef](#)]
40. Gao, C.; Luan, Y.; Yu, J.-C.; Ma, Y. Effect of thermo-mechanical treatment process on microstructure and mechanical properties of 2A97 Al-Li alloy. *Trans. Nonferr. Met. Soc. China* **2014**, *24*, 2196–2202. [[CrossRef](#)]
41. Zheng, X.; Luo, P.; Yue, G.; Hu, Y. Analysis of microstructure and high-temperature tensile properties of 2060 Al-Li alloy strengthened by laser shock peening. *J. Alloys Compd.* **2021**, *860*, 158539. [[CrossRef](#)]